Biosensors and Bioelectronics 130 (2019) 125–131

Contents lists available at ScienceDirect

Biosensors and Bioelectronics

journal homepage: www.elsevier.com/locate/bios

# Enzymatic oxydate-triggered AgNPs etching: A novel signal-on photoelectrochemical immunosensing platform based on Ag@AgCl nanocubes loaded RGO plasmonic heterostructure

Juan Tang[a,*], Pengyuan Xiong[a], Yu Cheng[a], Ya Chen[a], Siwen Peng[a], Zhi-Qiang Zhu[b]

[a] Ministry of Education Key Laboratory of Functional Small Organic Molecule, Department of Chemistry and chemical engineering, Jiangxi Normal University, Nanchang 330022, PR China

[b] School of Chemistry, Biology and Material Science, East China University of Technology, Nanchang 330013, PR China

ARTICLE INFO

*Keywords:*
photoelectrochemical immunosensor
ochratoxin A
AgNPs etching
Ag@AgCl/RGO heterostructure

ABSTRACT

A well-defined Ag@AgCl nanocubes loaded on the reduced graphene oxide plasmonic heterostructure (Ag@AgCl/RGO) was facilely prepared by sacrificial salt-crystal-template process and ethylene glycol-assisted reduction. The Ag@AgCl/RGO heterostructure shows superior photocurrent response and stability under the visible light irradiation. The enhanced performance mainly attributes to the plasmon resonance effect of AgNPs by improving the absorbance and transfer of photogenerated electrons. Significantly, we observed that the photocurrent could be dramatically decreased with the introduction of $H_2O_2$ and experimental results demonstrated the etching effect of $H_2O_2$ to AgNPs should be responsible for this phenomenon. Inspired by this phenomenon, employing $H_2O_2$ that generated from glucose oxidase catalyzed glucose triggered AgNPs etching as a novel signal mode, an improved photoelectrochemical immunosensing platform was constructed by employing Ag@AgCl/RGO heterostructure as photoactive material. As a proof of concept application, the photoelectrochemical immunosensor employed for ochratoxin A (OTA) detection with competitive-type format and it exhibited excellent analytical performance. Under optimized conditions, the photocurrent increased with the concentration of target OTA in the dynamic range of 0.05 to 300 nM with a limit of detection (LOD) of 0.01 nM (4.0 pg $mL^{-1}$). The immunosensor also showed high sensitivity, good reproducibility, and satisfactory accuracy. Although the methodology proposed here focused on OTA sensing, it could flexibly extend to monitor other targets by replacing the corresponding bio-recognition elements. Thus, this work provides a new paradigm for designing novel photoelectrochemical biosensing mode based on the plasmonic metal/semiconductor heterostructure.

## 1. Introduction

Ochratoxins, the toxic metabolites generated by a variety of fungi species that can be found in contaminated agricultural products such as fruit juices, wine, dried fruits, and cereals. Among them, ochratoxin A (OTA) is the most dangerous contaminant because of its toxicity, teratogenicity, and carcinogenicity (Feng et al., 2018; Jiang et al., 2018). Furthermore, OTA induces a long-term damage effect on health as it is metabolized slowly with a long half-life (more than a month) in the body (Zhu et al., 2018). With the recognition of its serious threat, international organizations including the World Health Organization and the European Union have established regulatory levels for tolerable weekly intake and specified the maximum permitted levels of OTA in different food stuff. Apparently, sensitive monitoring level of OTA is especially important (Viter et al., 2018; Myndrul et al., 2018). Nowadays, many techniques including liquid chromatography coupled with tandem mass spectrometry or quantitative fluorescence detecting, thin-layer chromatography, and enzyme linked immunosorbent assay (ELISA) have been developed for OTA detection. Though these methods may possess advantages in accuracy and precision, they usually suffer from sophisticated instrumentation, professional operators, high cost of running, and complicated time-consuming, which inevitably limit their applications in some areas. Developing rapid and low-cost methods with high sensitivity and selectivity for quantitative OTA is still necessary.

Photoelectrochemical (PEC) biosensing, an innovative detection technique has gained considerable attention and been widely applied to environmental monitoring, food security analysis, and clinical

* Corresponding author.
*E-mail address:* juantang@jxnu.edu.cn (J. Tang).

https://doi.org/10.1016/j.bios.2019.01.014
Received 20 August 2018; Received in revised form 24 December 2018; Accepted 1 January 2019
Available online 15 January 2019
0956-5663/ 

diagnosis in the recent years (Shu and Tang, 2017b; Zhao et al., 2015). Compared with the traditional instrument analysis and chemical analysis, the PEC biosensing shows distinctive advantages in aspects of selectivity, operability, and cost. Especially, profiting from the different energy forms of the excitation signal and the detection signal, PEC biosensing exhibits natural high signal-to-noise ratio. Enormous progress has been made in this field, however, as a newly developed technique, PEC biosensing modes are basically related to the producing redox species, steric hindrance effect, and energy transfer effect (Shu et al., 2018a). Accordingly, the signal amplification strategies and sensing formats are not sufficiently flexible to meet the various detecting needs. Developing detection modes based on novel signal-transduction principles with improved detection sensitivity and simplified procedures is significant (Ren et al., 2017b). On the other hand, quantification detection is achieved by monitoring the change of photocurrent for the most PEC biosensing. The photocurrent is generated from the photoelectric transformation involving electron excitation and transfer within the photoactive materials under light illumination with appropriate wavelength. Because the photoelectric transformation efficiency of photoactive materials directly determines the photocurrent intensity and indirectly effects on the sensitivity, the performance of PEC biosensors depends delicately on the quality and property of the photoactive materials.

Fortunately, enormous achievements of artificial photosynthesis made in the fields of energy, sensing, and environmental science provid theoretical basis and reference for the preparation of photoelectric materials as well as construction of PEC sensing (Shu et al., 2017a). Since the surface plasmon resonance of noble metal nanostructures (such as Au and Ag) was found to enhance the photoelectric conversion of large-bandgap photoelectric materials in the visible and NIR regions with good stability, it has been widely employed to construct various advance materials and for photophysical applications (Kochuveedu et al., 2013). Additionally, graphene, a two-dimensional carbon nanosheet with the high carrier mobility, could serve as atomic thickness substrate to function nanomaterials and to modulate the carrier transport for further improving photoactivity as well as biosensing performance (Yue et al., 2017; Zhu et al., 2017; Geleta et al., 2018; Ren et al., 2017a, 2017c; Xing et al., 2018; Yang et al., 2017a, 2017b).

Herein, reduced graphene oxide (RGO) sheet loading Ag@AgCl heterostructure (Ag@AgCl/RGO) was prepared and subsequently, it was used for constructing high sensitivity plasmon-enhanced PEC biosensor. RGO nanosheets serve as substrate for *in situ* growth of Ag@AgCl nanoparticles and improve the charge separation as well as transportation. Experimental results demonstrated that the prepared Ag@AgCl/RGO heterostructure exhibited excellent photocurrent response and stability under visible light irradiation and the sensitive response originated from the distinctive plasmon resonance effect of Ag nanoparticles (AgNPs). Destroying AgNPs within the Ag@AgCl/RGO heterostructure by introducing $H_2O_2$ could essentially decreases the photocurrent response. Inspired by the decisive role of AgNPs to the photocurrent under visible light irradiation, a highly sensitive photoelectrochemical immunosensor for OTA was constructed based on the enzymatic oxydate ($H_2O_2$)-triggered AgNPs etching. The immunosensor with the novel signaling model achieved excellent performance, implying the bright prospects in the PEC bioassay.

## 2. Experimental

### 2.1. Chemicals and materials

Ochratoxin A (OTA), glucose oxidase (GOx), bovine serum albumin (BSA, 96–99 wt%) and OTA-BSA bioconjugate were acquired from Sigma-Aldrich (Shanghai, China). Monoclonal antibody anti-OTA (mAb) was obtained from Immunechem (Burnaby, Canada). The high-binding polystyrene microplate was purchased from Greiner Bio-One (Frickenhausen, 705071, Germany). Acetate buffer solution (ABS, 0.1 M) and phosphate buffer solution (PBS, 0.1 M) with various pH-values were prepared by mixing their corresponding acid and salt solution. Other reagents obtained from Sinopharm Chemical Reagent Co., Ltd. (Shanghai, China) and Fuchen Chemicals (Tianjin, China) were analysis of pure and used as received.

### 2.2. Preparation of AgCl/GO nanocomposite and Ag@AgCl/RGO heterostructure

The synthetic method referenced from the previous report with a slight modification (Tang et al., 2013). GO was prepared in advance with the typical modified Hummer's method (Zhu et al., 2010). Polyvinylpyrrolidone (PVP, Mr ≈ 58,000) (0.1 g) was added into 100 mL of GO ethanol suspension (0.05 mg $mL^{-1}$) and treated ultrasonically for 10 min. Under magnetic stirring, NaCl saturated aqueous solution (0.4 mL) was quickly injected into the GO suspension. $AgNO_3$ (0.169 g) ethanolic solution (30 mL) containing PVP (1.0 g) was added into the above suspension and stirred for 24 h to obtain AgCl/GO nanocomposite. Subsequently, the obtained AgCl/GO was transfer into ethylene glycol (40 mL) and heated at 160 °C for 40 min in an oil bath under constant stir. The samples were washed with deionized water for several times and dried in an oven at 60 °C for 6 h

### 2.3. Fabrication of Ag@AgCl/RGO heterostructure modified electrode

Prior to modification, ITO (indium tin oxide, 10 × 50 × 2.2 mm) electrodes were cleaned in acetone and ultrapure water with the acid of ultrasonic treatment and then a waterproof tape with a round hole (6.0 mm in diameter) was pasted onto the conductive side of the electrode. Aqueous dispersion of Ag@AgCl/RGO (1 mg $mL^{-1}$) was dropped onto the round hole on the electrode and dried at 60 °C. Repeat previous step, rinsing electrodes for further use after chitosan solution (20 μL, 0.01 mg $mL^{-1}$) was added and naturally dried at RT.

### 2.4. Conjugation of OTA-BSA with GOx (OTA-BSA-GOx)

The typical process was concluded as the following steps: Initially, GOx (150 μL, 400 μg $mL^{-1}$) and OTA-BSA (50 μL, 200 μg $mL^{-1}$) were mixed with $Na_2CO_3$ solution (800 μL, 10 mM, pH 8.4) containing glucose (5 mM) and swayed gently for 0.5 h at room temperature on a shaker. Then, glutaraldehyde (0.1 mL, 25 wt%) was added into the above mixture and further incubated in a refrigerator (4 °C) for 12 h. Subsequently, adjusting the mixture pH to 6.4 and purifying it by ultrafiltration to remove the unreacted substrates. The acquired OTA-BSA-GOx conjugate was re-dispersed in ABS solution (2.0 mL, 10 mM, pH 6.4) containing sodium azide (0.1 wt%) and held in a refrigerator for later use.

### 2.5. Photocurrent measurement based on split-type immunosensing platform

To perform the competitive immunoreaction and PEC detection, firstly, monoclonal antibody anti-OTA (mAb, 10 μg $mL^{-1}$) in $Na_2CO_3$ solution (pH 9.6) was added into microplate (50 μL per well) followed by covered with plastic film and incubate for 12 h to immobilize the capture antibody onto microplate. Secondly, the plates blocked with skimmed milk solution in ABS (5%, pH 7.4, 300 μL per well) for 1 h at 37 °C. Thirdly, the OTA standard solutions (20 μL) with various concentrations (or practical samples) mixed with the equivalent volume of OTA-BSA-GOx and were immediately added to the mAb coated microplate. At the end of each step, the microplate was washed three times with ABS (pH 7.4). After incubation for 1 h at 37 °C, ABS buffer (150 μL, pH 5.0) containing glucose (4 mM) was injected into the washed microplate and reacted for 16 min to generate $H_2O_2$. Subsequently, transferring reaction solution (6 μL) from the microplate to the Ag@AgCl/RGO heterostructure modified electrode and further reacted for 8 min. Finally, the photocurrent response of the washed

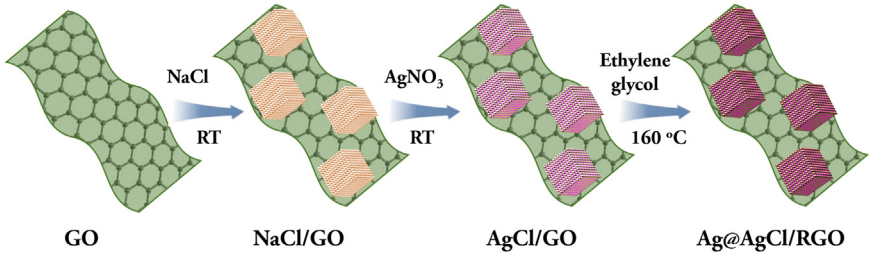


**Scheme 1.** Schematic illustration of the preparation of Ag@AgCl/RGO heterostructure with the sacrificial salt-crystal-template process and ethylene glycol-assisted reduction.

modified electrode was measured by an electrochemical workstation (CHI 680D) that equipped with a 500 W Xe lamp and a 420 nm cutoff filter (NBET, Beijing, China) with the applied potential of 0.1 V. $NaSO_4$ solution (0.1 M) was used as electrolyte and platinum wire and saturated calomel were used as the counter electrode and reference electrode, respectively. All detection was performed three-parallel experiment.

## 3. Results and discussion

### 3.1. Characterization of Ag@AgCl/RGO heterostructure

The Ag@AgCl/RGO heterostructure was facilely synthesized by the sacrificial salt-crystal-template (SCT) process and subsequent ethylene glycol-assisted reduction (EGR) as illustrated in Scheme 1. The effective ion exchange diffusion reaction between $Ag^+$ and NaCl nanograins causes a rapid growth of AgCl on the GO nanosheets (NaCl as the template). Subsequently, ethylene glycol, a common solvent and reductant, reduced GO and partial $Ag^+$ in the AgCl into RGO and AgNPs under heating conditions, respectively. The forming process of the heterostructure could be effectively monitored by Raman spectra (Renishaw invia Raman System) and X-ray diffraction (XRD, Shimadzu LabX XRD-6000) analysis. The purified product formed in the SCT process (Fig. 1A, curve *b*) exhibited two feature peaks of carbon material (G band around 1580 $cm^{-1}$ and D band around 1350 $cm^{-1}$) and an obvious Raman bands (180–300 $cm^{-1}$, curve *a*) of AgCl (Von Der Osten, 1974). In XRD analysis, this product (Fig. 1B, curve *b*) showed standard diffraction peak of AgCl (curve *a*) (JCPDS file: 31–1238) and a clear diffraction peak ($2\theta = 11.1°$) of GO, indicating the formation of AgCl nanograins in this process and without change for GO (Shu et al., 2018b). However, after EGR treatment, the purified product exhibited a significant change. The intensity ratio ($I_D/I_G$) of G band to D band in the characteristic Raman of Ag@AgCl/RGO (curve *c*) dramatically increased compared with that of AgCl/GO. Interestingly, the intensities of all bands were enhanced obviously after the EGR. The enhancement of Raman signal may attribute to the surface-enhanced Raman scattering (SERS) effect of AgNPs reduced from AgCl (Zhang et al., 2011). It also revealed that the AgNPs reduced on the surface of AgCl and closely adjacent to graphene, which could effectively affect electronic structure in plasmonic photoelectric system. Consistent with the Raman result, the XRD diffraction peak of GO disappeared completely and a new peak ($2\theta = 21.2°$) corresponding to RGO and weak diffraction peaks indexing to the metallic Ag (JCPDS file: 65-2871) appeared after EGR process. At the same time, no apparent peaks belonged to other impure phases such as $Ag_xO$ were observed, primarily suggesting that the obtained product was composed of graphene, metallic Ag, and AgCl.

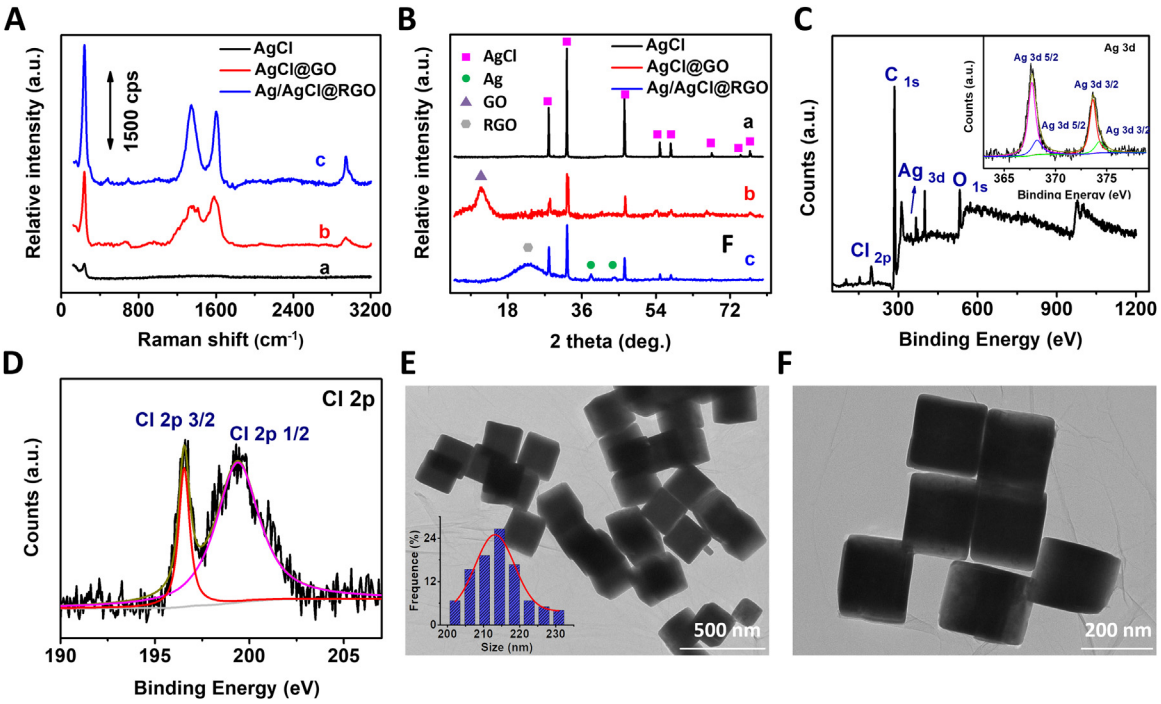


**Fig. 1.** (A) Raman spectra and (B) XRD patterns of nanocomposites; (C) XPS spectrum of the Ag@AgCl/RGO heterostructure [inset: high resolution XPS spectra of Ag 3d]; (D) high resolution XPS spectra of Cl 2p; (E) typical TEM images [insert: the corresponding size distributions] and (F) magnified TEM images of Ag@AgCl/RGO heterostructure.

These obvious changes indicated that the reduction of GO and generation of silver nanoparticles in the oil bath process. To further confirm the surface component and chemical states of the obtained product, X-ray photoelectron spectroscopy (XPS, VG Scientific ESCALAB 250 spectrometer) was performed and the results were shown in Fig. 1C. The four major elements (C, O, Ag, and Cl) were observed in the survey scan spectrum. Significantly, the spectrum of Ag 3d (Fig. 1C, inset) showed two peaks located at 367.3 eV and 373.3 eV, which could be deconvoluted into two sets of double peaks by a Gaussian distribution. The main peaks centered at 367.6 and 373.7 eV ascribed to Ag 3d5/2 and Ag 3d3/2 of AgCl, respectively. Two weak peaks centered at 368.2 eV and 374.3 eV attributed to Ag 3d5/2 and Ag 3d3/2 of AgNPs, respectively. Additionally, the two bands of Cl 2p3/2 and Cl 2p1/2 with binding energies of 197.6 and 199.25 eV were observed, respectively (Fig. 1D). The XPS results further confirm the formation of Ag@AgCl/RGO from the component and chemical states. Finally, the morphology was intuitively revealed by transmission electron microscopy (TEM, H-7650, Hitachi Instruments, Japan) and scanning electron microscopy (SEM, Quanta 250). The SEM image clearly showed that the cubic Ag@AgCl nanoparticles distributed on the GO nanosheets with micrometer-long wrinkles (Fig. S1) These Ag@AgCl nanocubes possessed clearly defined edges and rough surface. The TEM images also revealed that these well-separated Ag@AgCl/RGO with homogeneous size (the average edge length of Ag@AgCl nanocubes was 205 nm) and they were enwrapped by gauze-like GO sheets with obvious wrinkles, as shown in Fig. 2 E and F. The uniform size and regular morphology of Ag@AgCl nanocubes effectively ensure the reproducibility and stability of subsequent application.

### 3.2. Photoelectrochemical properties of Ag@AgCl/RGO

Here, to explore the photoelectric response of the prepared materials to visible light ($\lambda > 420$ nm), the transient photocurrent was recorded. Significant differences between the photocurrent intensity before (curve *d*) and after (curve *a*) EGR was observed, demonstrating the generation of AgNPs and RGO could essential improve the photocurrent (Fig. 2A). Interestingly, diametrically opposed to the previous reports that the photocurrent of photoactive material could be improved in the presence of $H_2O_2$, (Shu et al., 2016b, 2015) the $H_2O_2$ dramatically decreased the photocurrent of Ag@AgCl/RGO and the decrease level associated with the concentration of $H_2O_2$. Similar result was also reflected by photodegradation test with methylene blue (MB) dye as probe (Shu et al., 2016a). As shown in Fig. 2B, the color and absorbance of MB were basically unchanged after irradiation under visible light for 40 min in the presence of AgCl/GO (curve *b*). Conversely, there were obvious loss of color and absorbance of MB with the Ag@AgCl/RGO serving as photocatalyst under the identical photocatalysis conditions, implying improved visible light catalysis activity of Ag@AgCl/RGO (curve *c*). However, the catalytic activity of Ag@AgCl/RGO would also be disappeared after treated with small quantities of $H_2O_2$, which was consistent with the photocurrent measure. Based on the experimental phenomena and previous reports, the enhanced photocurrent under the visible light irradiation should be ascribe to the LSPR of AgNPs (Solarska et al., 2010; Chen et al., 2015; Wang et al., 2017). As shown in Fig. 2C, the Schottky junctions were established first at the contact interface with the *in-situ* reduction of AgNPs. When a photon with the wavelength matching with the intrinsic frequency of electron oscillation strike the surface, electromagnetic fields can be significantly confined and amplified in the vicinity of AgNPs. The decay of excited surface plasmon generates hot electrons with higher negative potential. These hot electrons inject into conduction band (CB) of AgCl, which ultimately results in photocurrent increase. This LSPR enhanced photocurrent mechanism of AgNPs is analogous to the dye sensitization in dye-sensitized solar cells. Since the $H_2O_2$ could effectively oxidation-etch AgNPs into $Ag^+$, we speculated that the Ag@AgCl/RGO heterostructure was destroyed by $H_2O_2$ and formed AgCl/RGO (Ma et al., 2016; Wang et al., 2014). Because of the wide band gap of AgCl (indirect band gap of 3.25 eV and direct band gap of 5.15 eV), the AgCl/RGO has weak response to the visible light, leading the photocurrent decrease with the addition of $H_2O_2$. To prove above speculation, morphology and crystal structure of Ag@AgCl/RGO heterostructure treated with $H_2O_2$ was investigated first. As shown in Fig. 2D, RGO remained

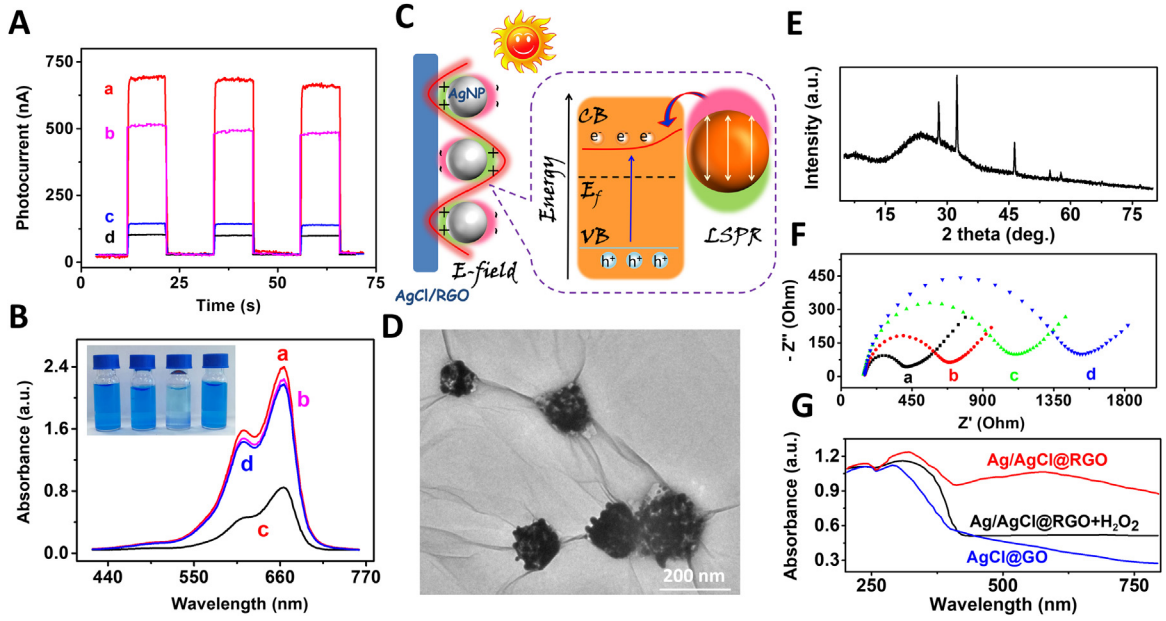


**Fig. 2.** (A) Photocurrent responses of Ag@AgCl/RGO/ITO (a), Ag@AgCl/RGO/ITO treated with 5 μM of $H_2O_2$ (b) and 0.1 mM of $H_2O_2$ (c) for 2 min, and AgCl/GO ITO (d); (B) UV–vis adsorption spectra of MB in the absence of photocatalyst (a) and in the presence of AgCl/GO (b), Ag@AgCl/RGO (c), and Ag@AgCl/RGO treated with $H_2O_2$ (d) [inset: photograph of the MB solution after photocatalytic degradation, from left are *a* to *d*]; (C) schematic illustration of LSPR enhancing photocurrent response within the Ag@AgCl/RGO heterostructure; (D) TEM image and (E) XRD pattern of Ag@AgCl/RGO heterostructure treated with $H_2O_2$; and (G) UV–vis diffuse-reflectance spectra of nanocomposites; (F) Nyquist diagrams for ITO (a), Ag@AgCl/RGO (b), Ag@AgCl/RGO treated with $H_2O_2$ (c) and AgCl/GO (d) in 5.0 mM $Fe(CN)_6^{4-/3-}$ containing 0.1 M KCl (the fitting Randle equivalent circuit was illustrated in Fig. S2).

the original shape while the cubic shape of Ag@AgCl become more irregular and many holes could be observed. The XRD result showed no substantial change but the diffraction peaks of metallic Ag disappeared (Fig. 2E). These results powerfully indicated the etching effect of $H_2O_2$ on AgNPs within the Ag@AgCl/RGO heterostructure. Generally, the typical PEC processes of photoelectric materials include light excitation and photogenerated carrier transferring. Thus, it is reasonable to explore the inhibitory effect of $H_2O_2$ to photocurrent from light absorption and charge transfer. The effect of etching AgNPs on the electron transportation and spectral absorption were revealed by electrochemical impedance spectroscopy and UV − vis − diffuse-reflectance spectra (Shimadzu UV-2450 spectrophotometer). Due to the reduction of GO and generation of AgNPs on the AgCl, the resistance of Ag@AgCl/RGO was smaller compared with that of the AgCl/GO (Fig. 2F), implying the direct contact interface existed between Ag@AgCl and RGO could enhance the electron transfer. In contrast, etching AgNPs that dispersed on the surface of Ag@AgCl nanocubes could destroy the interfacial contact and affect the electrons transportation, resulting the increase of the resistance (curve *c*). Significantly different from AgCl/GO samples that mainly exhibited adsorption near the UV region, the Ag@AgCl/RGO showed distinct absorption in visible region (Fig. 2G). The reason might be ascribed to that the localized surface plasmon state of AgNPs deposited within the Ag@AgCl nanocubes lies in the visible region. Namely, the increased absorption of visible light by the Ag@AgCl/RGO mainly originates from AgNPs. However, after treated with $H_2O_2$, the absorbance of Ag@AgCl/RGO in the visible region essentially decreased, which should ascribe to the etching effect of $H_2O_2$ to AgNPs.

### 3.3. Design of PEC immunosensor for OTA

The plasmonic Ag@AgCl/RGO heterostructure with enhanced PEC response coupling with the etching effect of $H_2O_2$ on plasmonic AgNPs may provide a novel signaling mode for developing an improved PEC sensing platform. To verify the feasibility of this signaling mode and as a proof of concept, a signal-on PEC immunosensor for OTA was proposed as illustrated in Scheme 2. Employing a typical competitive immunoassay format, the immunoreaction including an immunorecognition and enzyme-catalyzed process was performed on anti-OTA capture antibody (mAb)-immobilized microplates with glucose oxidase (GOx)-labeled OTA-bovine serum albumin (OTA-BSA) bioconjugate (GOx-OTA-BSA) as the signal tag. With the formation of immunocomplexes in microplates, the $H_2O_2$ generated from the carried GOx catalyzed oxidation of glucose. The generated $H_2O_2$ etched the AgNPs destroying the Ag@AgCl/RGO heterostructure and thus changing the photocurrent signal. The photocurrent variations directly associated with the generated $H_2O_2$ and indirectly reflect the target OTA concentration.

### 3.4. Optimization of experimental conditions

In order to achieve a better detection performance for OTA, the vital experimental conditions were optimized first by the variable-controlling approach. The all optimization was implemented at a constant concentration of OTA (0.5 nM). Because the photocurrent was extinguished by enzymatic oxidate ($H_2O_2$)-triggered etching reaction, the time for GOx catalytic reaction and AgNPs etching process would directly affect the response. As shown in Fig. 3A and B, the photocurrent decreased with both time for catalytic reaction and etching process and eventually tended to level off. Excessively extending time did not apparently decrease the photocurrent of immunosensor. To improve detection efficiency, 16 and 8 min were utilized for catalytic reaction and etching process because this time allocation could obtain a high response in the shortest possible time. Apart from reaction time, the pH of buffer solution for GOx catalytic reaction also optimized. As can be seen from Fig. 3C, the minimum photocurrent was obtained at pH of 5.0 for GOx catalytic reaction since the higher or lower pH would inhibit the bioactivity of GOx. Actually, the slightly acidic environment also favors etching process. Thus, buffer solution with pH of 5.0 was chosen for GOx catalytic reaction.

### 3.5. Analytical performance of Ag@AgCl/RGO-based PEC immunosensing platform for OTA

Subsequently, under the optimal detection conditions, the immunosensing platform based on the $H_2O_2$ etching Ag@AgCl/RGO heterostructure was utilized to detect OTA standard samples with various concentrations. As shown in Fig. 4A, the photocurrent of the immunosensor increased with the OTA concentration raised and the intensities were well linear to the logarithmic values of OTA concentration in the range from 0.05 nM to 300 nM. The regression equation was fitted to $I = 339.74 + 128.51 \times \lg [C_{OTA}]$ ($R^2 = 0.989$, n = 8, where $I$ (nA) is the peak value of the photocurrent and $C_{[OTA]}$ (nM) is the concentration of OTA, respectively) and the limit of detection derived to be 0.01 nM based on a signal-to-noise ration of 3σ/slope (where σ is the standard deviation of 11 parallel detection for a blank sample). In term of the linear range and the detection limit, the proposed PEC

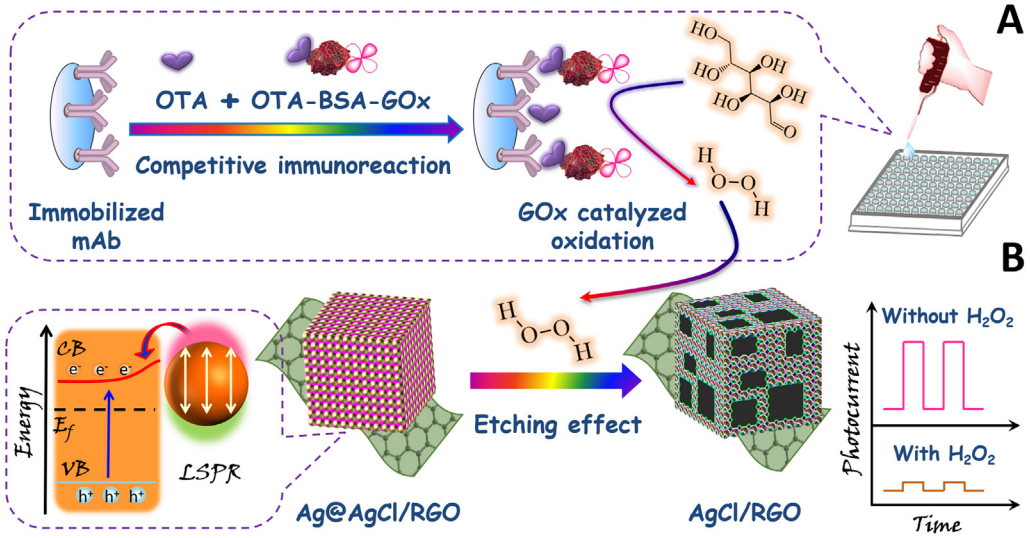


**Scheme 2.** Schematic illustration of the PEC immunosensing platform for OTA based on Ag@AgCl/RGO heterostructure coupling with enzymatic oxidate ($H_2O_2$)-triggered etching signaling mode.

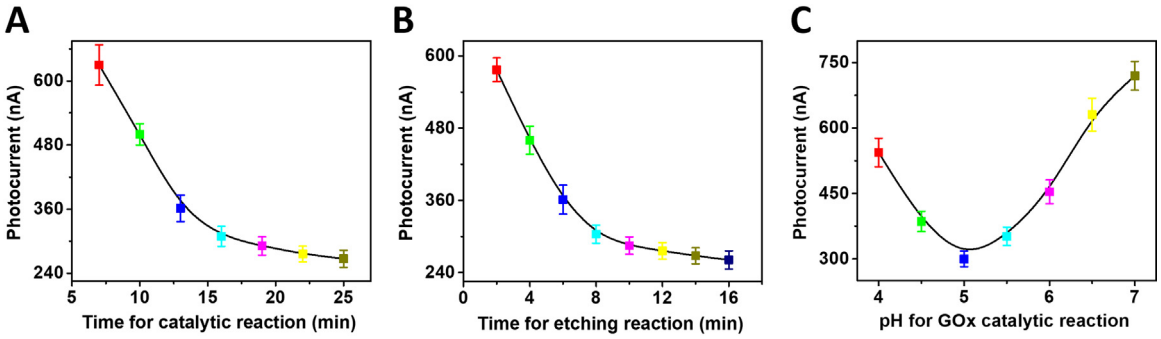


**Fig. 3.** The optimization of the time for (A) catalytic reaction and (B) etching process; (C) the optimization of the pH for GOx catalytic reaction (0.5 nM OTA standard sample used in all these cases).

immunosensor based on the novel signal mode showed certain advantages compared with previous reports (Karczmarczyk et al., 2017; Lv et al., 2017, 2016; Rivas et al., 2015; Chu et al., 2016; Chen et al., 2014; Sun et al., 2017; Liu et al., 2015), as listed in Table S1.

The specificity was a vital parameter needed to be considered and it was examined by challenging this platform against other possible coexist toxins (10 nM) including ochratoxin B (OTB), brevetoxin B (BTB), and vomitoxin (DON). Both the photocurrent responses to OTB, BTB, and DON was similar to that of blank, but the significantly increased photocurrent could be observed once trace amounts of OTA (0.5 nM) was added. Additionally, there was little difference between the responses to OTA and the mixture samples. This result powerfully illustrated the excellent specificity of the proposed immunosensing platform.

To evaluate the reproducibility and stability, OTA standard samples with various concentrations (0.5, 10 and 100 nM) were repeatedly detected for 3 times and the relative standard deviations were 5.1%, 7.6% and 6.2% for intra-assay and 6.9%, 9.1% and 8.6% for inter-assay, respectively. The prepared immunosensors placed in a refrigerator (4 °C) for two weeks and the average of photocurrent response still remained above 90% of its initially response. These results indicated the excellent reproducibility and long-term stability of the immunosensor for OTA detection and also verified the possibility of batch preparation.

### 3.6. Analysis of real samples and evaluation of method accuracy

Generally, the feasibility and reliability of a newly developed biosensor are especially important for the detection of real samples, especially involving complex matrixes. Here, the proposed PEC immunosensor challenged to analyze the OTA in spiked juices samples and spiked red wine samples to evaluate the feasibility in practical application. The concentrations of OTA calculated from the calibration curve depicted in Fig. 4B was compared with the commercial OTA ELISA kit

**Table 1**
Accuracy and reliability evaluation of the proposed PEC immunosensor for OTA in real samples.

| Sample no.[a] | Method accuracy [conc. (mean ± SD (RSD), nM, $n$ = 3)][b] | | $t_{exp}$ |
|---|---|---|---|
| | PEC immunosensor | OTA ELISA kit | |
| 1 | 2.1 ± 0.1 (4.8%) | 2.2 ± 0.1 (4.5%) | 1.23 |
| 2 | 4.8 ± 0.4 (8.3%) | 4.9 ± 0.3 (6.1%) | 0.35 |
| 3 | 9.6 ± 0.8 (7.3%) | 9.5 ± 0.6 (6.3%) | 0.18 |
| 4 | 19.4 ± 1.8 (9.3%) | 21.2 ± 0.97 (4.6%) | 1.53 |
| 5 | 50.4 ± 3.8 (7.5%) | 51.8 ± 2.1 (4.1%) | 0.56 |
| 6 | 104.4 ± 5.9 (5.6%) | 98.1 ± 5.2 (5.3%) | 1.41 |

[a] Samples no. 1–3 were detected in juices and sample no. 4–6 were detected in red wine.
[b] Each value is mean of three replicate detection.

with an unpaired Student's $t$-test and the statistical results were list in Table 1. The all $t_{exp}$ were less than $t_{crit}$ ($t_{crit}$ [0.05,4] = 2.78) indicating that there was no great difference between the two methods at the confidence level of 95%. Using average values obtained by the PEC immunosensor as ordinate and average values obtained by the ELISA kit as abscissa, a regression equation was fitted as $y = 1.345 + 0.942x$ ($R^2 = 0.997$) and the slope of the regression equation approaches to 1. Thus, the proposed PEC immunosensor could be employed as a reliable, sensitive and accurate technique for OTA detection.

## 4. Conclusions

In summary, the Ag@AgCl nanocubes loaded onto RGO plasmonic heterostructure was prepared by a facile synthesis. The Ag@AgCl/RGO heterostructure exhibited significantly enhanced PEC responses and stability in the visible light region. Experimental results showed the direct interfacial contact existed between the Ag@AgCl and reduced

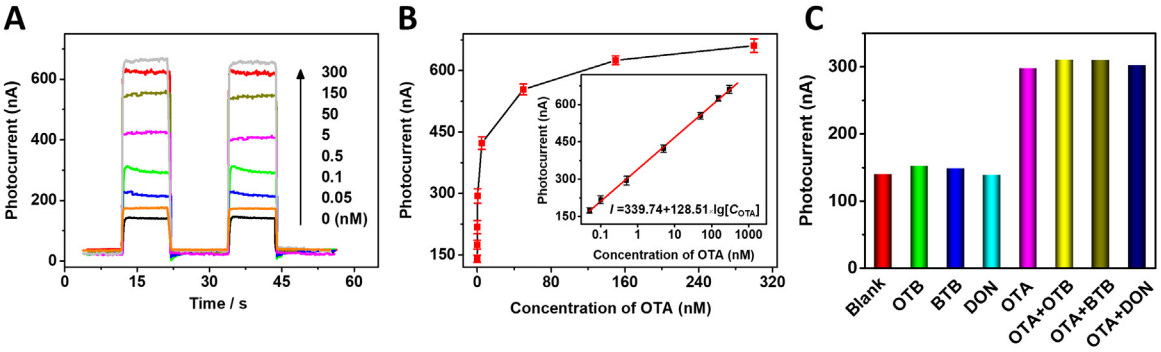


**Fig. 4.** (A) Photocurrent responses of Ag@AgCl/RGO-based PEC immunosensing platform toward target OTA with various concentrations; (B) The photocurrent intensity versus concentrations of OTA ranging from 0 to 300 nM (inset: the corresponding calibration curve of photocurrent intensity and the logarithmic value of OTA concentration); (D) the specificity evaluation of the proposed immunosensing platform.

graphene oxide. Ag@AgCl/RGO heterostructure has strong absorbance and excellent photocurrent response in the visible light region because of the surface plasmon resonance (SPR) of AgNPs. Once strongly plasmonic AgNPs was etched by the $H_2O_2$, several times decrease of photocurrent could be observed. Inspired by this phenomenon, employing etching effect of $H_2O_2$ to Ag@AgCl/RGO plasmonic heterostructure as a novel signal mode, subsequently, an improved PEC immunosensing platform was constructed and the quantitative relationship between the photocurrent response and the concentration of OTA was established. Compared with many detection methodologies for OTA, this PEC immunosensor based on the novel signaling mode exhibited great advantages in detection limit and linear range. The selectively, reproducibility and precision were carefully evaluated and were acceptable. The PEC immunosensing platform can flexibly extend to monitor other targets by replacing the corresponding bio-recognition elements and thereby represents a versatile sensing protocol, which makes it a bright prospect in the area of bioanalysis.

## Acknowledgements

This work was financially supported by the National Natural Science Foundation of China (21864013, 21505060), the Foundation of Jiangxi Educational Committee (GJJ150327), the Science Foundation of Jiangxi Province (20161BAB213073), Scientific Research Foundation of Jiangxi Normal University, The Open Project Program of Key Laboratory of Functional Small Organic Molecule, Ministry of Education, Jiangxi Normal University (No. KLFS-KF-201710), Outstanding Youth Funds of Jiangxi Normal University.

## Appendix A. Supporting information

Supplementary data associated with this article can be found in the online version at doi:10.1016/j.bios.2019.01.014.

## References

Chen, H.Y., Lin, M.H., Wang, C.Y., Chang, Y.M., Gwo, S., 2015. J. Am. Chem. Soc. 137, 13698–13705.
Chen, J., Zhang, X., Cai, S., Wu, D., Chen, M., Wang, S., Zhang, J., 2014. Biosens. Bioelectron. 57, 226–231.
Chu, X., Dou, X., Liang, R., Li, M., Kong, W., Yang, X., Luo, J., Yang, M., Zhao, M., 2016. Nanoscale 8, 4127–4133.
Feng, J., Li, Y., Gao, Z., Lv, H., Zhang, X., Fan, D., Wei, Q., 2018. Biosens. Bioelectron. 99, 14–20.
Geleta, G.S., Zhao, Z., Wang, Z., 2018. J. Anal. Test. 2, 20.
Jiang, C., Lan, L., Yao, Y., Zhao, F., Ping, J., 2018. TrAC Trends Anal. Chem. 102, 236–249.
Karczmarczyk, A., Haupt, K., Feller, K.H., 2017. Talanta 166, 193–197.
Kochuveedu, S.T., Jang, Y.H., Kim, D.H., 2013. Chem. Soc. Rev. 42, 8467–8493.
Liu, R., Huang, Y., Ma, Y., Jia, S., Gao, M., Li, J., Zhang, H., Xu, D., Wu, Min, Chen, Yan, Zhu, Z., Yang, C., 2015. ACS Appl. Mater. Interfaces 7, 6982–6990.
Lv, L., Cui, C., Liang, C., Quan, W., Wang, S., Guo, Z., 2016. Food Control 60, 296–301.
Lv, L., Li, D., Liu, R., Cui, C., Guo, Z., 2017. Sens. Actuators B-Chem. 246, 647–652.
Ma, J.L., Yin, B.C., Wu, X., Ye, B.C., 2016. Anal. Chem. 89, 1323–1328.
Myndrul, V., Viter, R., Savchuk, M., Shpyrka, N., Erts, D., Jevdokimovs, D., Silamiķelis, V., Smyntyna, V., Ramanavicius, A., Iatsunskyi, I., 2018. Biosens. Bioelectron. 102, 661–667.
Ren, X., Ma, H., Zhang, T., Zhang, Y., Yan, T., Du, B., Wei, Q., 2017a. ACS Appl. Mater. Interfaces 9, 37637–37644.
Ren, X., Yan, J., Wu, D., Wei, Q., Wan, Y., 2017b. ACS Sens. 2, 1267–1271.
Ren, X., Zhang, T., Wu, D., Yan, T., Pang, X., Du, B., Luo, W., Wei, Q., 2017c. Biosens. Bioelectron. 94, 694–700.
Rivas, L., Mayorga-Martinez, C.C., Quesada-González, D., Zamora-Gálvez, A., de la Escosura-Muñiz, A., Merkoçi, A., 2015. Anal. Chem. 87, 5167–5172.
Shu, J., Qiu, Z., Lin, Z., Cai, G., Yang, H., Tang, D., 2016a. Anal. Chem. 88, 12539–12546.
Shu, J., Qiu, Z., Lv, S., Zhang, K., Tang, D., 2018a. Anal. Chem. 90, 2425–2429.
Shu, J., Qiu, Z., Lv, S., Zhang, K., Tang, D., 2017a. Anal. Chem. 89, 11135–11142.
Shu, J., Qiu, Z., Tang, D., 2018b. Anal. Chem. 90, 9691–9694.
Shu, J., Qiu, Z., Zhou, Q., Lin, Y., Lu, M., Tang, D., 2016b. Anal. Chem. 88, 2958–2966.
Shu, J., Qiu, Z., Zhuang, J., Xu, M., Tang, D., 2015. ACS Appl. Mater. Interfaces 7, 23812–23818.
Shu, J., Tang, D., 2017b. Chem. Asian J. 12, 2780–2789.
Sun, A.L., Zhang, Y.F., Sun, G.P., Wang, X.N., Tang, D., 2017. Biosens. Bioelectron. 89, 659–665.
Solarska, R., Królikowska, A., Augustyński, J., 2010. Angew. Chem., Int. Ed. 49, 7980–7983.
Tang, Y., Jiang, Z., Xing, G., Li, A., Kanhere, P.D., Zhang, Y., Sum, T.C., Li, S., Chen, X., Dong, Z., Chen, Z., 2013. Adv. Funct. Mater. 23, 2932–2940.
Viter, R., Savchuk, M., Iatsunskyi, I., Pietralik, Z., Starodub, N., Shpyrka, N., Ramanaviciene, A., Ramanavicius, A., 2018. Biosens. Bioelectron. 99, 237–243.
Von Der Osten, W., 1974. Phys. Rev. B 9, 789–793.
Wang, D., Sherman, B.D., Farnum, B.H., Sheridan, M.V., Marquard, S.L., Eberhart, M.S., Dares, C.J., Meyer, T.J., 2017. PNAS 114, 9809–9813.
Wang, L., Zheng, J., Li, Y., Yang, S., Liu, C., Xiao, Y., Li, J., Cao, Zhong, Yang, R., 2014. Anal. Chem. 86, 12348–12354.
Xing, B., Zhu, W., Zheng, X., Zhu, Y., Wei, Q., Wu, D., 2018. Sens. Actuators B-Chem. 265, 403–411.
Yang, L., Li, Y., Zhang, Y., Fan, D., Pang, X., Wei, Q., Du, B., 2017a. ACS Appl. Mater. Interfaces 9, 35260–35267.
Yang, L., Zhu, W., Ren, X., Khan, M.S., Zhang, Y., Du, B., Wei, Q., 2017b. Biosens. Bioelectron. 91, 842–848.
Yue, Z., Liu, A., Zhang, C., Huang, J., Zhu, M., Du, Y., Yang, P., 2017. Appl. Catal., B. 201, 202–210.
Zhang, H., Fan, X., Quan, X., Chen, S., Yu, H., 2011. Environ. Sci. Technol. 45, 5731–5736.
Zhao, W.W., Xu, J.J., Chen, H.Y., 2015. Chem. Soc. Rev. 44, 729–741.
Zhu, C., Du, D., Lin, Y., 2017. Biosens. Bioelectron. 89, 43–55.
Zhu, X., Kou, F., Xu, H., Han, Y., Yang, G., Huang, X., Chen, W., Chi, Y., Lin, Z., 2018. Sens. Actuators B-Chem. 270, 263–269.
Zhu, Y., Murali, S., Cai, W., Li, X., Suk, J.W., Potts, J.R., Ruoff, R.S., 2010. Adv. Mater. 22, 3906–3924.